The Theory of Critical Distances for Predicting the Static Failure of Double-Lap Bolted Joints With Conventional and Additively Manufactured 316L Stainless Steel Inner Plates

ALMUHANNA, Hasan <http://orcid.org/0000-0001-7486-6307>, TORELLI, Giacomo and SUSMEL, Luca <http://orcid.org/0000-0001-7753-9176>

Fatigue & Fracture of Engineering Materials & Structures

WILEY

FFEMS Fatigue & Fracture of Engineering Materials & Structures

ORIGINAL ARTICLE OPEN ACCESS

The Theory of Critical Distances for Predicting the Static Failure of Double-Lap Bolted Joints With Conventional and Additively Manufactured 316L Stainless Steel Inner Plates

Hasan Almuhanna[1] | Giacomo Torelli[1] | Luca Susmel[2]

[1]School of Mechanical, Aerospace and Civil Engineering, The University of Sheffield, Sheffield, UK | [2]School of Engineering and Built Environment, Sheffield Hallam University, Sheffield, UK

Correspondence: Luca Susmel (l.susmel@shu.ac.uk)

Received: 31 March 2026 | **Revised:** 18 May 2026 | **Accepted:** 12 June 2026

Keywords: bolted joints | ductile material | static failure | theory of critical distances

ABSTRACT

This study assesses the accuracy of the theory of critical distances applied in the form of the point method in predicting the static strength of 316L stainless steel double-lap shear bolted connections under static tensile loading. Single- and double-bolt configurations were tested using inner plates manufactured from conventional material and from additively manufactured material, namely wire arc additive manufacturing and selective laser melting. The additively manufactured plates were assessed in both machined and as-built conditions and extracted at different printing orientations. Treating the bolt hole as a stress concentrator, linear elastic finite element stress fields were postprocessed to determine the point method effective stress from stress–distance curves extracted along different paths relative to the loading direction. The point method, calibrated using an inherent stress and a characteristic length estimated from 2-mm-thick conventional notched plates, provided generally good predictions for both conventional and additively manufactured plates. However, the prediction accuracy decreased for thicker as-built wire arc additively manufactured plates. Recalibrating the point method using wire arc additive manufacturing notched specimens with a comparable mean thickness improved the predictions for the thicker wire arc additively manufactured plates; however, a nonconservative bias remained. These findings confirm that the point method parameters calibrated using plain and notched specimens can be transferred to bolted joint assemblies.

1 | Introduction

The most common solutions for joining structural steel components are welding, bolts, and rivets. These typical connecting methods are robust in ensuring the overall reliability of structural assemblies. Nevertheless, the advantage of bolts over other solutions is that the structural parts connected by bolts can easily be disassembled and then reused. This further encouraged researchers in the field to investigate and utilize various innovative additive manufacturing (AM) techniques for the fabrication of bolted connections, leading to a growing body of research exploring their structural performance and potential applications [1–8]. In addition, these advances have opened new possibilities for optimizing structural steel connections using AM technologies, allowing for tailored designs that were not feasible with conventional manufacturing approaches [9]. For example, topology-optimized wire arc additively manufactured (WAAM) bolted head plates [10] and optimized metal AM connections in lightweight steel framing [11] have been proposed, highlighting possible future applications involving complex connection geometries and improved stiffness and strength. A recent review has also identified metal AM, particularly WAAM, as a promising technology for steel construction, especially where large-scale automated fabrication, reduced material waste, and the production or strengthening of complex structural components are required

Summary

- TCD point method predicts the static strength of 316L bolted joints well.
- Consistent accuracy for conventional and AM plates of similar thickness.
- FE-based stress fields enable robust and reliable TCD assessments.
- Recalibration enhances accuracy for WAAM plates across configurations.

[12]. However, wider adoption in structural steel applications remains limited by challenges associated with defects related to the manufacturing process, surface condition, residual stresses, anisotropic material behavior, and the lack of structural design guidance [12]. In a previous work conducted by the authors [13], a comprehensive failure behavior examination was carried out, starting with the assessment of conventionally produced (CON) 316L stainless steel inner plates as reference specimens. This was followed by testing inner plates produced through AM, specifically using WAAM and selective laser melting (SLM), in order to evaluate their potential as viable alternatives.

As far as design is concerned, evaluating the impact of various design variables on stress concentration and plate failure in bolted connections is crucial for ensuring structural integrity and durability. Traditionally, this evaluation has heavily relied on nonlinear finite element (FE) models [14], which offer a detailed and accurate representation of complex stress distributions and failure mechanisms under different loading conditions. For instance, ductile fracture in bolted connections has been numerically simulated using nonlinear FE analysis combined with a ductile fracture criterion and a damage evolution rule [15]. In contrast, the use of linear elastic models, which simplify bolt holes as stress concentrators and treat bolted connections as notched components, has not yet been systematically explored. Although linear elastic models offer a computationally less demanding solution, they can nonetheless provide valuable insights into stress concentration phenomena, provided that the problem is addressed using a reliable methodology. To address this knowledge gap, the Theory of Critical Distances (TCD) was employed in this study to assess the static strength of double-lap shear bolted connections within a linear elastic framework. The TCD is a set of approaches for predicting fracture at stress or strain concentrators of various types using a material-specific critical distance, and it provides a practical framework for evaluating strength and failure in engineering applications [16].

The TCD postulates that the static strength of notched and cracked components can be estimated by directly postprocessing the stress fields near the stress raisers being assessed; under Mode I loading, the TCD states that fracture occurs when a critical distance-related effective stress, σ_{eff}, exceeds the material's inherent strength, σ_0 [17–23]. A distinctive feature of the TCD is that σ_{eff} can be evaluated using a linear elastic constitutive law, thereby greatly simplifying the design problem. However, material-specific factors influence the relationship between σ_0 and the ultimate tensile strength, σ_{UTS}. For ductile materials with significant plastic deformation preceding final failure, σ_0 is typically higher than σ_{UTS} [18]. Brittle and quasi-brittle materials generally have σ_0 approaching σ_{UTS} [23].

There are four different ways to determine the effective stress according to the TCD, that is, the Point Method (PM), Line Method, Area Method, and Volume Method [16]. To apply the TCD in the form of either the PM or the Line Method, the first step is to define the so-called focus path. The focus path is typically defined as a straight line emanating from the hot spot (assumed to coincide with the crack initiation point) and aligned with the crack propagation direction, that is, the direction experiencing the maximum damage extent [16].

Once the focus path has been defined, in the PM the critical stress is taken at a distance equal to $L/2$ from the hot spot associated with the stress/strain concentrator under assessment, where L is the TCD material characteristic length (an experimentally determined material length scale). In contrast, the line method calculates σ_{eff} by averaging the stress along the focus path over a length equal to $2L$. Finally, the area method and the volume method calculate σ_{eff} by averaging the stress over a semicircular area (with radius $\approx 1.32\,L$) and a hemispherical volume (with radius $\approx 1.54\,L$), respectively [16].

In this study, the PM was selected because of its simplicity and suitability for ductile materials such as 316L stainless steel [22, 24]. Following the shear tests, the PM was applied by postprocessing the local linear elastic FE stress fields obtained from numerical models replicating the bolted connection tests on CON inner plates. The stress–distance focus path for the PM was defined at the hole midthickness edge within the hot spot region, centered on the experimentally observed crack initiation location in the tested inner plates. To account for the observed variation in crack paths, stress–distance curves were extracted from the initiation point along three directions: perpendicular, diagonal, and parallel to the loading direction, and the PM predictions were evaluated for each path. Additionally, the path most closely aligned with the experimentally observed crack direction was identified and used for comparison.

The values of L and σ_0 were first calibrated from two notched specimens manufactured from the same material as the CON plates, following the standard procedure described in detail in Section 4.2. These material constants were then used in conjunction with the PM to postprocess the FE models of the CON inner plates. The same L–σ_0 pairing was subsequently applied to the FE models of inner plates produced by WAAM and SLM to assess transferability across manufacturing methods. A further assessment was performed for the as-built WAAM (WAAM-AB) inner plates by calibrating an additional L–σ_0 pairing using WAAM notched specimens with a comparable mean thickness.

2 | Reference Experiments

This section presents the material properties, design, and key results from an experimental program discussed in detail in Ref.

[13]. The key goal of this initial experimental investigation was to perform a detailed failure analysis of bolted joints containing both conventional and AM plates. These results will then be used in the following sections of the paper as a basis for assessment via TCD.

Prior to testing the bolted specimens, a series of coupon tests was conducted in accordance with ASTM E8/E8M [25], covering both CON specimens and AM specimens produced by WAAM and SLM. The coupons were tested in both machined and as-built conditions. For WAAM specimens, surface undulations and different extraction orientations were considered, whereas for SLM specimens, the effect of deposition direction was evaluated. The key mechanical properties of the tested materials, including elastic modulus, E, yield stress, $\sigma_{0.2}$, and ultimate tensile stress, σ_{UTS}, are summarized in Table 1. In the specimen designations, M refers to machined, and AB indicates as-built. The reported angle specifies the orientation of the specimen relative to the deposition or extraction direction. It can be noted from Table 1 that some modulus of elasticity, E, values are relatively low. As discussed in detail in [13], the comparatively low E values measured for some AM specimens were mainly associated with manufacturing-related effects and specimen orientation.

The experimental setup and procedures for the double-lap shear tests are described below. Each connection consisted of two 2-mm-thick inner test plates and two 4-mm-thick outer plates, assembled using fully threaded grade 10.9 M6 high-strength bolts. The bolt holes had a diameter of 6.6 mm to provide adequate clearance. The increased thickness of the outer plates was intended not only to withstand the applied loads but also to minimize secondary bending during testing and ensure that failure occurred in the inner plates, which were the primary focus of the investigation. For the WAAM-AB plates, non-threaded grade 12.9 M8 bolts were used instead, with the hole size increased to 8.4 mm, and the outer plate thickness increased to 8 mm to accommodate the larger bolts and the increased mean thicknesses and surface undulations. For the SLM specimens, the designation M indicates that the rough surface was removed by machining, without altering the overall thickness. The test setup is illustrated in Figure 1, whereas the design details and the measured failure capacities for each configuration are summarized in Table 2 and Table 3 [13]. In these tables, the notation IP in the designation column refers to the inner plates: IP1 indicates plates tested in the single-bolt configuration, whereas IP2 denotes plates tested in the double-bolt configuration. The number that follows each designation identifies the specific specimen, corresponding to its unique set of geometrical variables. Similar to the coupons, additional identifiers specify the manufacturing method (CON, WAAM, or SLM) and, for AM plates, the deposition/extraction direction (e.g., 0° or 90°).

3 | Observed Cracking Behavior and Definition of the TCD Focus Paths

The location of crack initiation and propagation directions was identified by post-test inspection of CON, WAAM, and SLM specimens [13]. In all cases, the crack initiation occurred at the bolt hole edge on the loaded side within the bearing zone, where the bolt-to-hole contact produces localized damage and the highest stress concentration (Figure 2a–c). For CON plates, crack propagation typically followed the weakest ligament defined by the specimen geometry and relative dimensions, producing mainly straight tearing paths either parallel or perpendicular to the loading direction. Accordingly, the crack direction was not random but largely governed by the geometrical design of the specimen, which determined the weakest ligament and in turn led to well-defined, typical failure modes and tearing paths. For WAAM plates, cracking could deviate from this tendency, with several specimens additively manufactured at raster angles of 45° and 60° exhibiting a diagonal

TABLE 1 | Mechanical properties from coupon tests [13].

Designation	Modulus of elasticity, E (GPa)	Offset yield stress, $\sigma_{0.2}$ (MPa)	Ultimate stress, σ_{UTS} (MPa)
CON	184	488	667
WAAM-M-0°	143	288	521
WAAM-M-45°	185	324	552
WAAM-M-60°	160	297	530
WAAM-M-90°	103	281	562
WAAM-AB-0°	124	278	493
WAAM-AB-45°	119	282	544
WAAM-AB-60°	139	323	566
WAAM-AB-90°	91	273	493
SLM-AB-0°	160	520	627
SLM-AB-45°	126	422	562
SLM-AB-90°	120	419	554

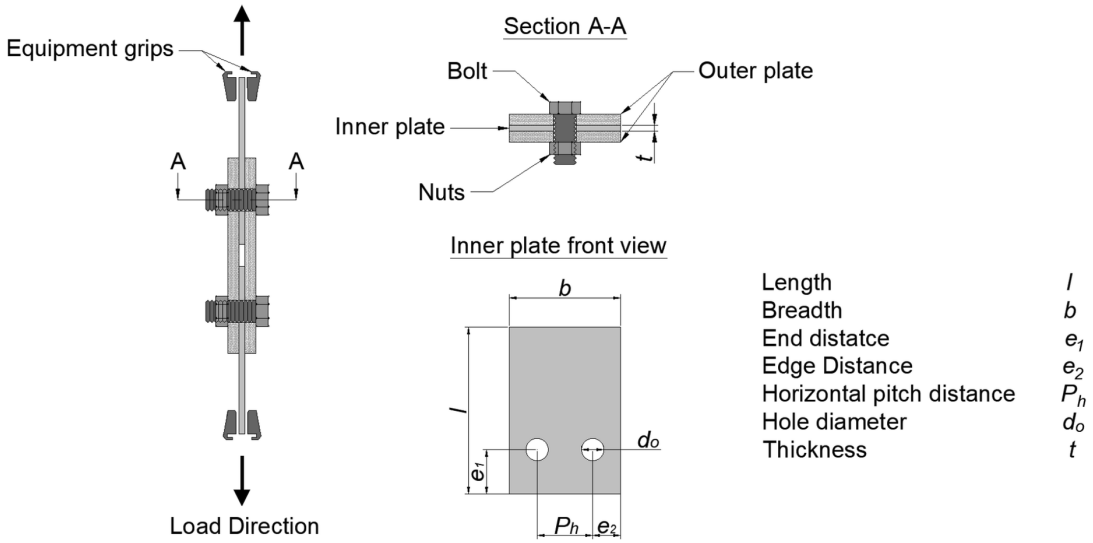

FIGURE 1 | Test setup for double-lap shear bolted connections, illustrating the two-bolt configuration.

crack trajectory. This is attributed to the WAAM layer morphology and its orientation relative to the loading direction, which can guide crack growth and promote inclined propagation. In contrast, the SLM specimens showed cracking behavior more consistent with that of the CON specimens, with the crack initiation location and propagation direction remaining broadly similar across the tested configurations and showing minimal sensitivity to surface condition and print direction. Based on the observed cracking behavior, three representative focus paths were considered for each specimen in the TCD analyses discussed below: perpendicular, diagonal, and parallel. The link between the observed cracking behavior and the focus path directions is illustrated schematically in Figure 2d.

4 | Application of the TCD

4.1 | Methodology

In the standard formulation of the PM, once the material's characteristic length, L, and the focus path are determined, the effective stress, σ_{eff}, is defined as the stress value located at a distance of $L/2$ from the tip of the notch or crack being assessed [18, 26] (Figure 3a,b):

$$\sigma_{\text{eff}} = \sigma_{\text{VM}}\left(\theta = 0, r = \frac{L}{2}\right). \quad (1)$$

In Definition (1), σ_{VM} is von Mises equivalent stress, whereas θ and r are polar coordinates. Von Mises stress was employed in this study since previous work reported that, for ductile materials modeled by using a linear elastic constitutive law, it provides more accurate predictions than Tresca's criterion and the maximum principal stress criterion [20]. The characteristic length, L, can directly be estimated via the following well-known definition:

$$L = \frac{1}{\pi}\left(\frac{K_{IC}}{\sigma_0}\right)^2 \quad (2)$$

with K_{IC} being the plane strain fracture toughness, which is recommended to be determined experimentally in accordance with ASTM E399 [28].

As defined by Equation (2), determining the value of L is straightforward only when the inherent material strength, σ_0, is assumed equal the ultimate tensile strength, σ_{UTS}, and the value of K_{IC} is available. If this condition is not satisfied, a well-established alternative approach consists of calibrating the parameters from experimental results obtained by testing specimens containing notches of different sharpness [18]. This procedure is illustrated in Figure 3. According to the PM argument, the intersection point of two linear elastic stress–distance curves at incipient failure, derived from tests on notches of different sharpness, allows the direct estimation of σ_0 and L. The procedure summarized in Figure 3c was used in the present investigation to determine L.

4.2 | Characterization of σ_0 and L via the Two-Notch Approach

Two U-notched specimens were prepared using CON 316L stainless steel: one with a sharp notch with root radius, r_n, equal to 0.5 mm and the other with a blunt notch with $r_n = 1.5$ mm, as shown in Figure 4. Uniaxial tensile tests were conducted with a displacement rate of 1 mm/min. Two global load–displacement curves for the representative sharp notch test and the blunt notch test are shown in Figure 5a,b. These tests were followed by linear elastic three-dimensional FE simulations performed using FE commercial software ANSYS Mechanical [29]. The elastic modulus, $E = 184$ GPa, obtained from the CON coupon tests was used in the numerical analyses. Each specimen type was then modeled by progressively refining the mesh in the vicinity of the notch tip until convergence was achieved. The linear elastic stress–distance curves (in terms of von Mises equivalent stress) along the notch bisectors at the incipient failure condition were then extracted for both specimens. These curves were then combined (see Figure 5c), and the values of

TABLE 2 | Design details and ultimate load capacities of inner plates with single-bolt configuration [13].

Designation	Thickness, t (mm)	End distance, e_1 (mm)	Edge distance, e_2 (mm)	Breadth, b (mm)	Experimental ultimate load, F_{Exp} (kN)
IP1-1-CON	2	14	15	30	18.8
IP1-2-CON	2	13	15	30	18.1
IP1-3-CON	2	11	15	30	15.7
IP1-4-CON	2	8	15	30	11.3
IP1-5-CON	2	15	8	16	12.0
IP1-1-WAAM-M-0°	2	14	15	30	18.4
IP1-1-WAAM-M-45°	2	14	15	30	19.2
IP1-1-WAAM-M-60°	2	14	15	30	18.5
IP1-1-WAAM-M-90°	2	14	15	30	17.8
IP1-2-WAAM-M-0°	2	14	15	30	16.9
IP1-2-WAAM-M-45°	2	14	15	30	19.0
IP1-2-WAAM-M-60°	2	14	15	30	18.1
IP1-2-WAAM-M-90°	2	14	15	30	16.2
IP1-3-WAAM-M-0°	2	11	15	30	15.0
IP1-4-WAAM-M-0°	2	8	15	30	11.2
IP1-1-WAAM-AB-0°	5.4	14	15	30	44.3
IP1-2-WAAM-AB-0°	5.4	13	15	30	40.8
IP1-2-WAAM-AB-45°	5.3	13	15	30	41.6
IP1-2-WAAM-AB-60°	5.2	13	15	30	38.0
IP1-2-WAAM-AB-90°	5.2	13	15	30	41.6
IP1-3-WAAM-AB-0°	5.3	11	15	30	33.6
IP1-4-WAAM-AB-0°	5.4	8	15	30	23.8
IP1-5-WAAM-AB-0°	5.2	15	8	16	22.6
IP1-5-WAAM-AB-45°	5.4	15	8	16	23.9
IP1-5-WAAM-AB-60°	5.3	15	8	16	20.5
IP1-5-WAAM-AB-90°	5.3	15	8	16	23.0
IP1-1-SLM-M-0°	2	14	15	30	18.5
IP1-1-SLM-AB-0°	2	14	15	30	18.7
IP1-2-SLM-AB-0°	2	13	15	30	18.3
IP1-2-SLM-AB-45°	2	13	15	30	18.7
IP1-2-SLM-AB-90°	2	13	15	30	17.5
IP1-5-SLM-AB-0°	2	15	8	16	11.6
IP1-5-SLM-AB-45°	2	15	8	16	11.1
IP1-5-SLM-AB-90°	2	15	8	16	10.7

σ_0 and $L/2$ at the intersection were determined to be 1441 MPa and 0.22 mm, respectively. The obtained value of σ_0 is about twice the ultimate tensile stress, $\sigma_{UTS} = 667$ MPa, measured from the CON 316L stainless steel coupon tests. The obtained ratio between σ_0 and σ_{UTS}, of about 2, is consistent with the observations reported in David Taylor's book [16]. The values of σ_0 and $L/2$ obtained through this procedure were then used in the TCD assessment of the bolted connections.

TABLE 3 | Design details and ultimate load capacities of inner plates with double-bolt configuration [13].

Designation	Thickness, t (mm)	End distance, e_1 (mm)	Edge distance, e_2 (mm)	Horizontal pitch distance, p_h (mm)	Breadth, b (mm)	Experimental ultimate load, F_{Exp} (kN)
IP2-1-CON	2	12	12	16	40	27.3
IP2-2-CON	2	11	12	16	40	26.6
IP2-3-CON	2	8.2	12	16	40	23.1
IP2-4-CON	2	8	12	16	40	23.0
IP2-5-CON	2	7	12	16	40	21.1
IP2-6-CON	2	16	8	24	40	30.4
IP2-7-CON	2	15	11	18	40	32.1
IP2-1-WAAM-M-0°	2	12	12	16	40	26.3
IP2-1-WAAM-M-45°	2	12	12	16	40	27.4
IP2-1-WAAM-M-60°	2	12	12	16	40	26.8
IP2-1-WAAM-M-90°	2	12	12	16	40	25.3
IP2-2-WAAM-M-0°	2	11	12	16	40	27.3
IP2-3-WAAM-M-0°	2	8.2	12	16	40	23.8
IP2-3-WAAM-M-45°	2	8.2	12	16	40	24.4
IP2-3-WAAM-M-60°	2	8.2	12	16	40	23.3
IP2-3-WAAM-M-90°	2	8.2	12	16	40	21.6
IP2-4-WAAM-M-0°	2	8	12	16	40	23.1
IP2-5-WAAM-M-0°	2	7	12	16	40	20.7
IP2-7-WAAM-M-0°	2	8.2	12	16	40	31.4
IP2-2-WAAM-AB-0°	5.5	11	12	16	40	57.0
IP2-3-WAAM-AB-0°	5.6	8.2	12	16	40	49.5
IP2-3-WAAM-AB-45°	5.2	8.2	12	16	40	47.7
IP2-3-WAAM-AB-60°	5.5	8.2	12	16	40	48.9
IP2-3-WAAM-AB-90°	5.3	8.2	12	16	40	44.9
IP2-4-WAAM-AB-0°	5.0	8	12	16	40	47.6
IP2-5-WAAM-AB-0°	5.3	7	12	16	40	43.7
IP2-6-WAAM-AB-0°	5.4	16	8	24	40	70.8
IP2-6-WAAM-AB-45°	5.0	16	8	24	40	62.8
IP2-6-WAAM-AB-60°	5.3	16	8	24	40	61.8
IP2-6-WAAM-AB-90°	5.0	16	8	24	40	61.7
IP2-7-WAAM-AB-0°	5.4	8.2	12	16	40	70.8
IP2-7-SLM-M-0°	2	15	11	18	40	31.7
IP2-6-SLM-AB-0°	2	16	8	24	40	31.1
IP2-6-SLM-AB-45°	2	16	8	24	40	31.6
IP2-6-SLM-AB-90°	2	16	8	24	40	30.6
IP2-7-SLM-AB-0°	2	15	11	24	40	33.5

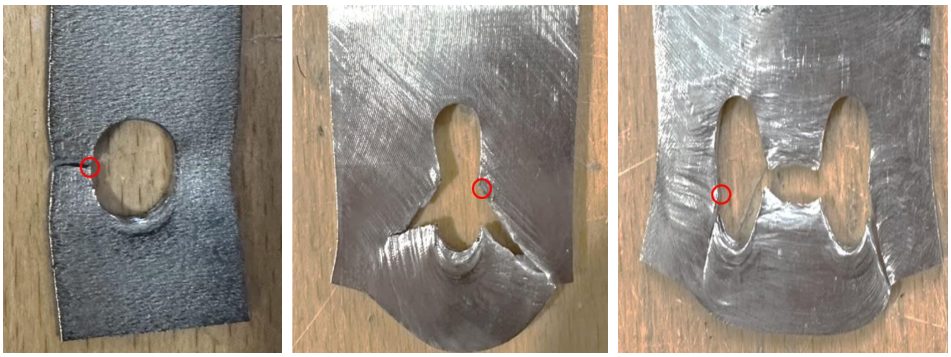

(a) IP1-5-SLM-AB-90° (b) IP1-1-WAAM-M-45° (c) IP2-2-WAAM-M-0°

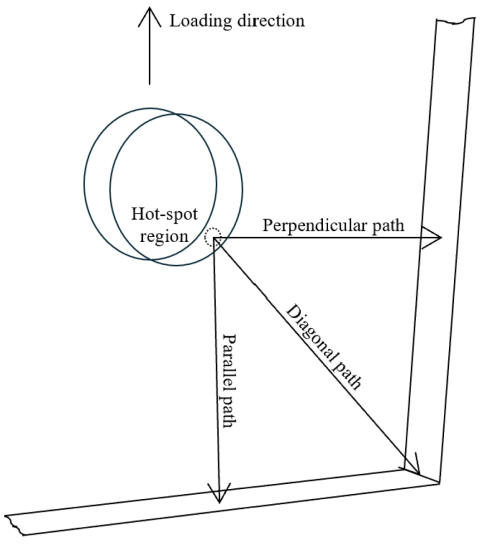

(d)

FIGURE 2 | Representative experimentally observed failures for selected (a) SLM and (b, c) WAAM specimens, showing the crack initiation point at the bolt hole edge (red circles) and the resulting crack paths [13]; (d) corresponding TCD focus paths from the crack initiation point relative to the loading direction. [Colour figure can be viewed at wileyonlinelibrary.com]

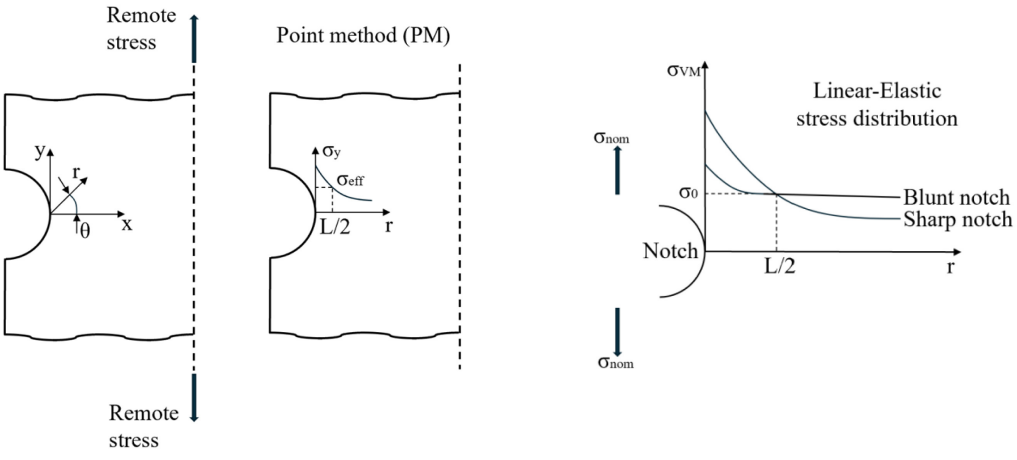

(a) (b) (c)

FIGURE 3 | Illustration of the point method (PM): (a) local polar coordinates, (b) effective stress evaluation at a distance $L/2$ from the notch root, and (c) determination of σ_0 and L from the intersection of the linear elastic stress curves for two notch types. (a) and (b) are adapted from [27], whereas (c) is adapted from [18]. [Colour figure can be viewed at wileyonlinelibrary.com]

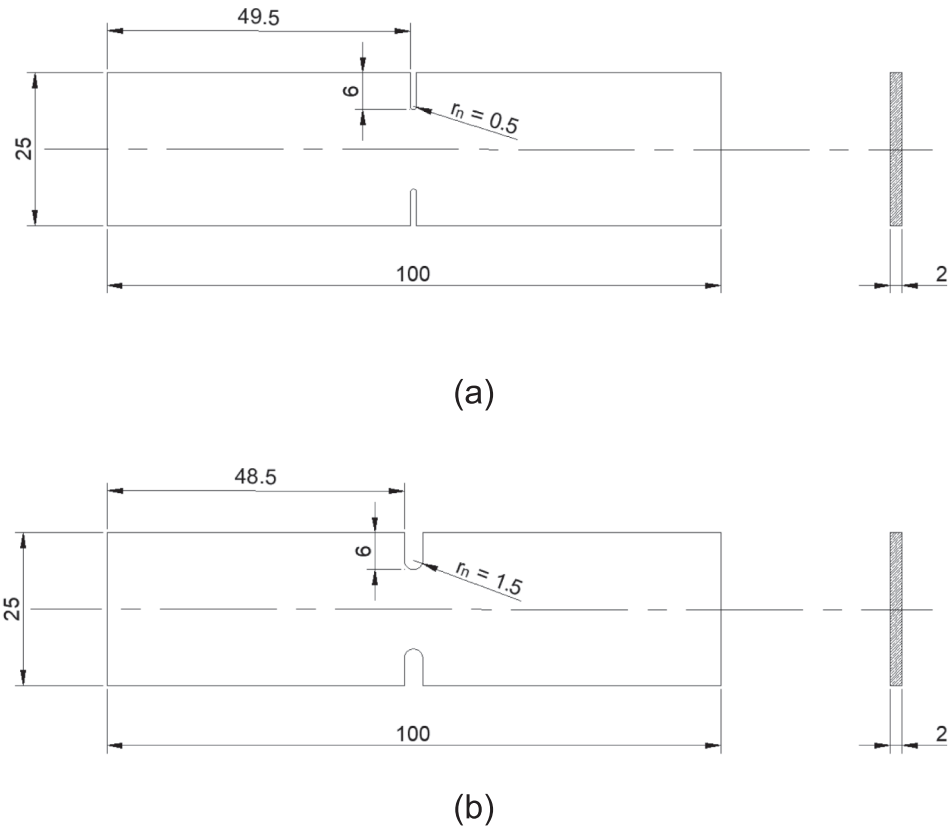

FIGURE 4 | Geometrical dimensions of the notched specimens (in millimeters): (a) sharp notch and (b) blunt notch.

To enable a further assessment under matching AM conditions, the same two-notch calibration procedure was also applied to WAAM-AB material. Two notched WAAM-AB plates, with the same dimensions as those of CON notched specimens, were tested. The specimens were extracted and tested only in the 0° direction. The mean measured thickness was 5.3 mm for the plate containing the blunt notch and 5.2 mm for the plate with the sharp notch.

The corresponding global load–displacement curves for the sharp and blunt notched specimens are shown in Figure 6a,b, respectively. The FE-derived stress–distance curves are reported in Figure 6c, from which the values of σ_0 and $L/2$ were estimated to be approximately 1345 MPa and 0.31 mm, respectively. Because of limited material availability, only two AM specimens could be tested. Although this did not allow any statistical assessment of variability, it was nevertheless possible to obtain an approximate estimate of the above parameters. The resulting ratio of σ_0 and σ_{UTS} is also higher than that obtained for the CON material, ranging from approximately 2.4 to 2.7 based on the WAAM-AB ultimate tensile stress values reported in Table 1. However, this range is considered reasonable, because the ratio of σ_0 and σ_{UTS} is expected to increase from unity for a fully brittle material as material ductility increases. Therefore, the value of approximately 2 reported by Taylor [16] should be regarded as a reference value rather than a fixed limit. The higher ratio obtained for the WAAM-AB specimens may also be influenced by the specific as-built morphology of the material, including surface undulations and local geometric irregularities.

4.3 | Finite Element Model Setup for Bolted Connections

The linear elastic stress fields in the vicinity of the bolt holes were obtained from three-dimensional FE models developed in ANSYS Mechanical (see Figure 7a,b) [29]. The reason for adopting 3D models was that, as mentioned in the previous section, the stress analysis was carried out in terms of von Mises equivalent stress. Accordingly, the relevant stress fields and the corresponding stress–distance curves were determined at the midsection of the tested plates, that is, at those sections experiencing the highest degree of stress triaxiality (although this remained limited due to the small thickness of the plates).

Initially, a standard detailed contact-based assembly model was adopted to replicate the experimental configuration as closely as practicable and to verify the sensitivity of the near-hole stress field to modeling assumptions. The model comprised the complete plate–bolt–nut assembly, with all interfaces represented through contact definitions. The IP1-1-CON configuration was used as the base model for the sensitivity studies on friction and mesh refinement. By using the assembly tool available in ANSYS [29], these components were combined into a full model without merging, enabling the specification of contact interactions. All relevant interfaces were defined as frictional, except between the bolt and nut, where a bonded contact was applied. This choice corresponded to the experimental setup, where a minimal tightening torque was used to align the plates and restrict movement in directions other than the applied load. Therefore,

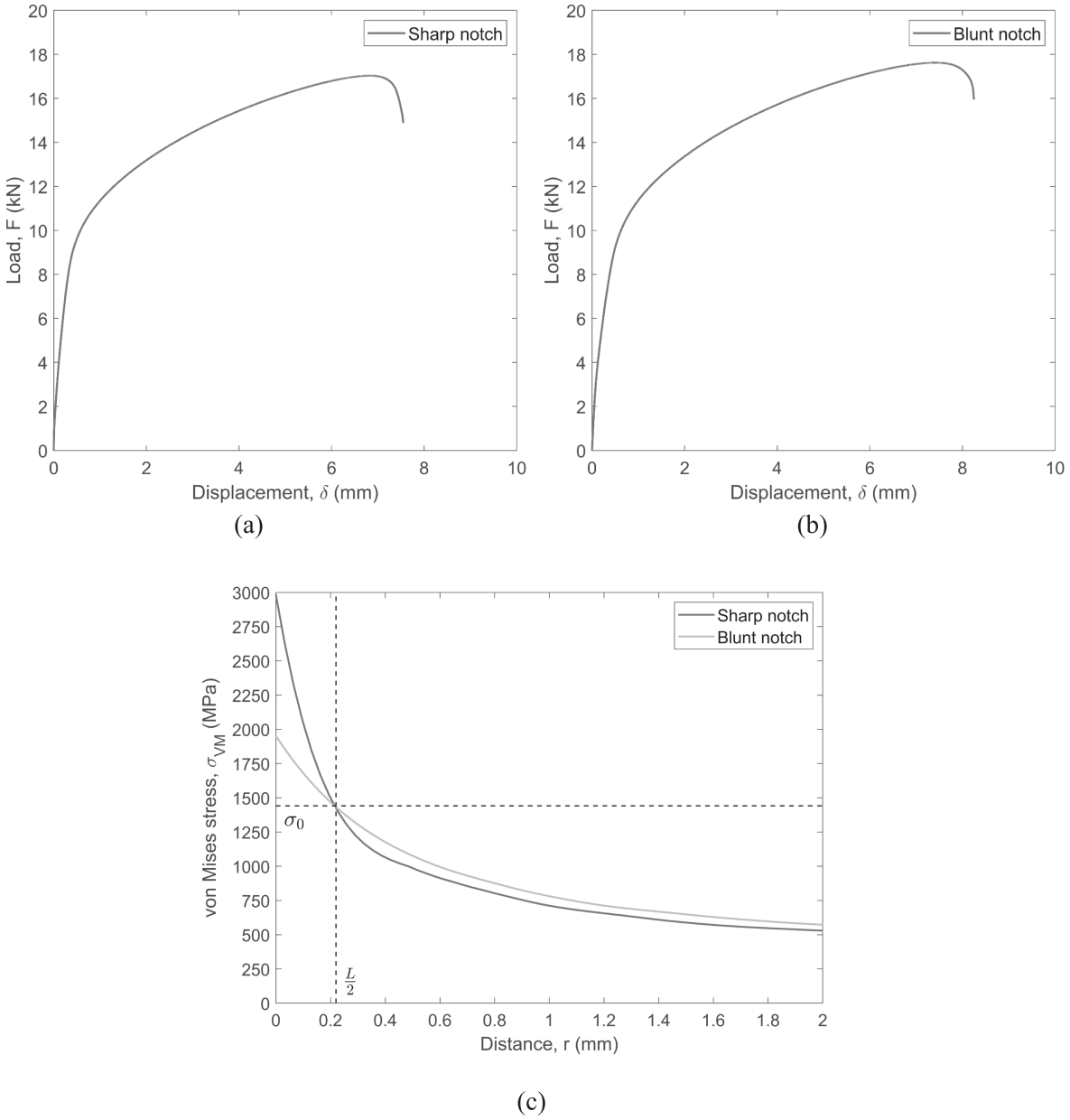

FIGURE 5 | Load–displacement curves for the CON notched specimens with a uniform thickness of 2 mm. (a) Sharp notch and (b) blunt notch; (c) corresponding FE stress–distance curves.

in the model, this bonded bolt–nut definition both prevented slip at the interface and provided adequate clamping without the need to model minimal bolt preload. This reduced unnecessary detail in the connection representation and ensured stable analysis, as the study focused on plate stress distribution rather than detailed preload behavior. The friction coefficient, μ, was investigated through a sensitivity study comparing $\mu = 0.15$, 0.20, and 0.25, which showed mean σ_{VM} differences below 1.7% over the stress–distance range from the edge of the inner plate hole. Because of the limited variability observed in the sensitivity study, and consistent with earlier FE studies on steel bolted joints [30, 31], the value of μ was taken as 0.20 for all models. The bolt shanks were designed as smooth cylinders with diameters equal to the nominal size, and the clearance between bolts and holes was omitted to avoid introducing contact errors. This simplification was adopted to obtain a stable and repeatable local stress field for the TCD assessment, although it may affect the initial bearing contact, local load transfer, and near-hole stress distribution.

As shown in Figure 7c, the mesh refinement tool was applied directly to the bolt hole edges. The circular geometry enabled the generation of a uniform, radially distributed fine mesh without the need for bias lines. A mesh sensitivity study was conducted on the IP1-1-CON inner plate model, with global element sizes of 1.2, 1.0, and 0.8 mm. The 0.8-mm mesh significantly increased computational time with only a 0.3% mean change in σ_{VM} over the stress–distance range between 1.0- and 0.8-mm mesh sizes. Therefore, a global element size of 1.0 mm was adopted, which, after local refinement, reduced the element size to approximately 0.3 mm around the holes. The outer plates, bolts, and nuts were meshed with a 2.0-mm element size.

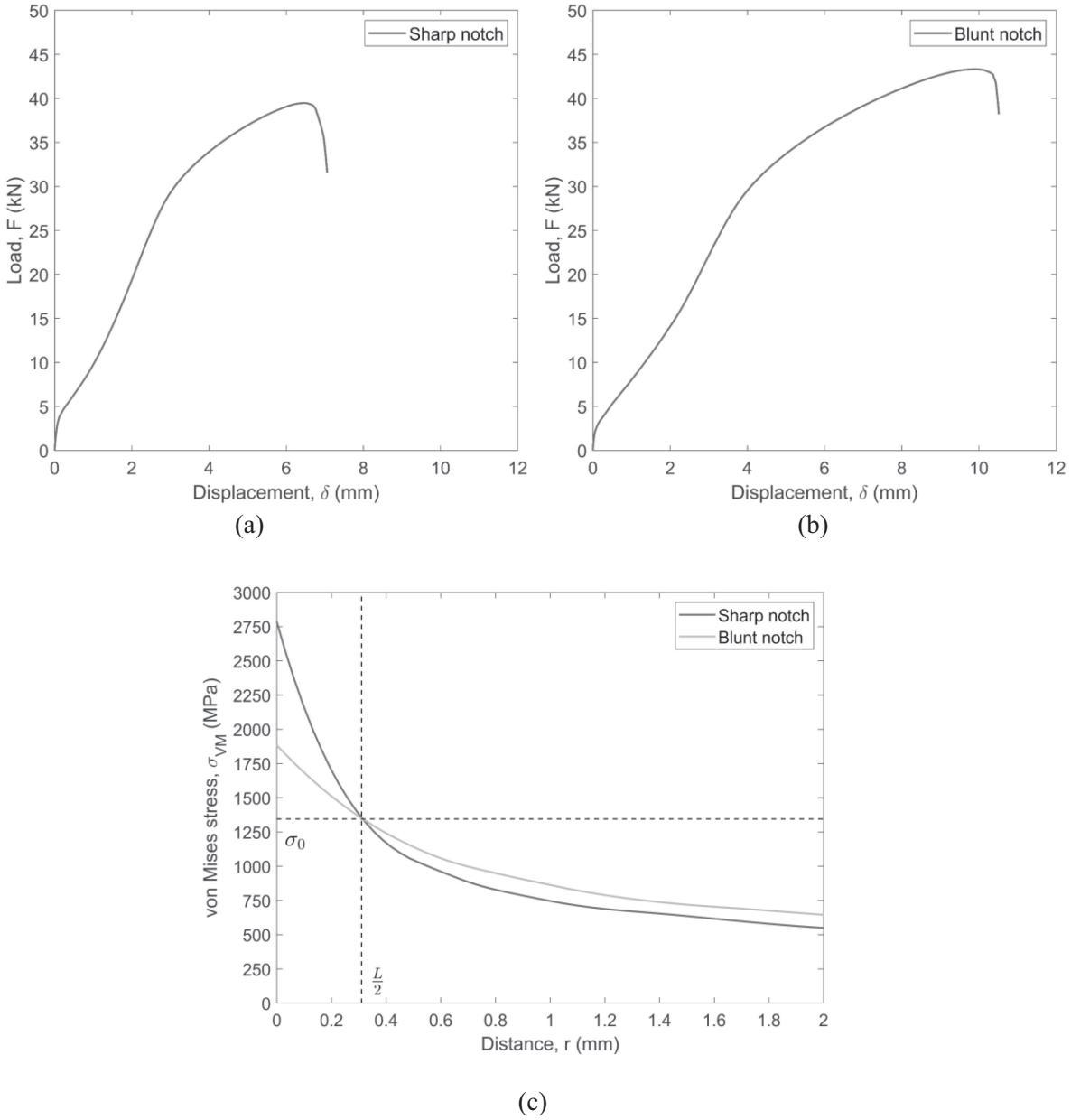

FIGURE 6 | Load–displacement curves for the WAAM-AB notched specimens. (a) Sharp notch and (b) blunt notch; (c) corresponding FE stress–distance curves.

Although the detailed contact-based assembly model provided a rigorous representation of the experimental configuration, it required long run times, which would have made processing the full dataset inefficient. A simplified model was therefore implemented to achieve a substantial reduction in run time while retaining the accuracy required for the TCD-based assessment. The simplified model (see Figure 8) consisted of a single inner plate with a cylindrical solid inserted through the bolt hole to represent the bolt shank. The frictional contact between the shank and the plate was kept at 0.2. The shank end faces were fully fixed, and the end face of the plate was subjected to the experimental load. The shank was extended by 1 mm beyond both plate faces so that the boundary conditions were applied away from the hole edge, avoiding artificial surface stress spikes and allowing a representative stress field through the hole thickness to develop.

Stress–distance curves were extracted through the plate midthickness along three paths relative to the loading direction: perpendicular, diagonal, and parallel (Figure 2d). For each path, the origin was defined at the experimentally observed crack initiation point on the hole edge, which was consistent with the FE hot spot corresponding to the maximum stress location. A direct comparison of the equivalent von Mises stress, σ_{VM}, along each path showed very close agreement between the full and simplified FE models (Figure 9). Along the perpendicular path, the simplified model differed from the full model at $L/2$ by only about 0.3%. Similar differences were observed for the other directions, with $\sigma_{VM}(L/2)$ differing by 0.3% for the diagonal path and by 1.0% for the parallel path. When averaged over a distance equal to L, the mean difference between the simplified and full models remained below 1% for all three focus path directions, with an overall mean absolute difference of about 0.6%.

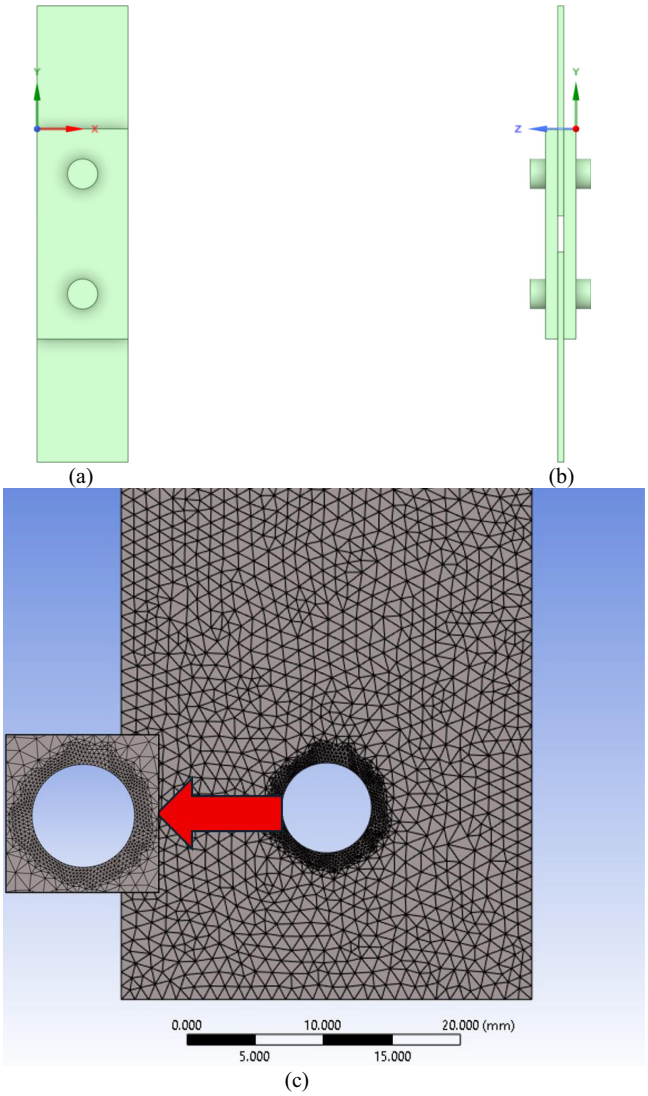

FIGURE 7 | A full 3D finite element model of the double-bolted connections: (a) front view, (b) side view, and (c) inner plate's tetrahedral mesh with a zoom into the refinement around the holes. [Colour figure can be viewed at wileyonlinelibrary.com]

FIGURE 8 | Simplified model showing a single inner plate with a cylindrical bolt shank inserted through the hole: (a) front view and (b) side view. [Colour figure can be viewed at wileyonlinelibrary.com]

This simplified model therefore eliminates most of the contact-related complexity and reduces the run time by approximately 83% while preserving the governing stress fields. Accordingly, the simplified numerical approach was thus adopted for all subsequent models.

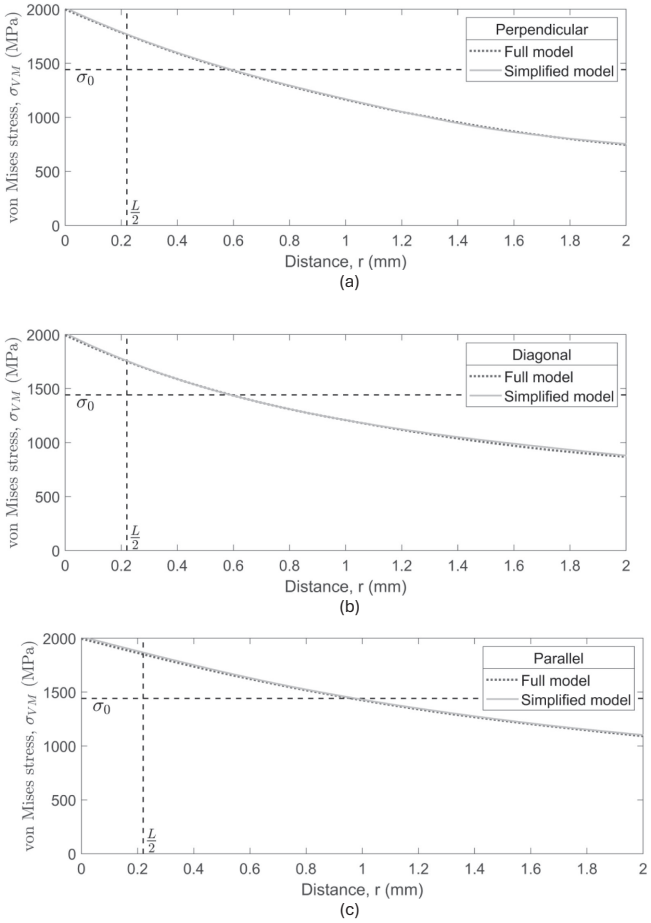

FIGURE 9 | Comparison of the full and simplified FE models for IP1-1-CON: (a) perpendicular, (b) diagonal, and (c) parallel paths.

Using the focus path definition introduced in Section 3 (Figure 2d), stress–distance curves for each specimen were extracted at the plate midthickness. The predicted hot spot was consistently located at the loaded hole edge, in good agreement with the experimentally observed crack initiation point. For each specimen, this experimentally identified point was therefore selected as the origin of the TCD focus paths. Figure 10 shows the corresponding FE contours for representative specimen cases, illustrating that this experimentally identified point lies within the hot spot location. The resulting effective stress, σ_{eff}, and the corresponding PM prediction accuracy were compared for each path. This will be discussed in the next sections.

4.4 | TCD-PM Assessment of CON Inner Plates

Following the results of Section 4.2, where the values of σ_0 and L were determined using the standard two-notch approach based on two CON specimens containing sharp and blunt notches, the predictive accuracy of the PM was assessed initially for the CON inner plates. The PM was applied to the corresponding stress–distance curves to evaluate the signed relative prediction error defined as follows:

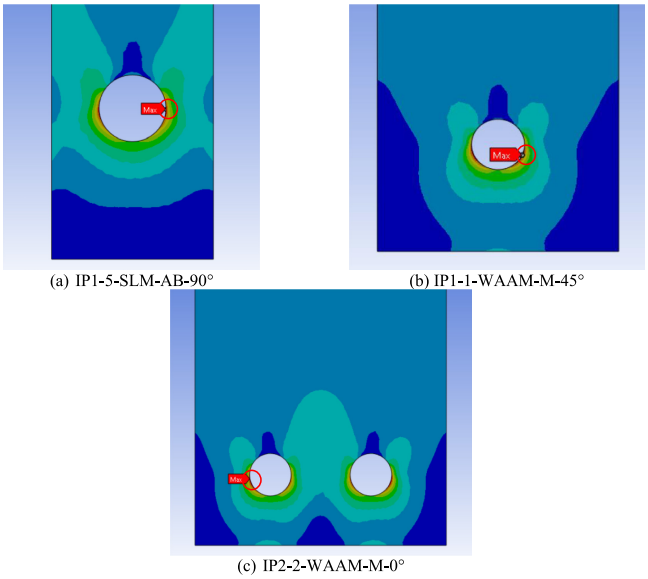

(a) IP1-5-SLM-AB-90° (b) IP1-1-WAAM-M-45°

(c) IP2-2-WAAM-M-0°

FIGURE 10 | The corresponding FE equivalent von Mises stress contours for representative specimen cases. The "Max" label indicates the location of the maximum σ_{VM} and is shown for reference, whereas the red circles mark the experimentally observed crack initiation point at the bolt hole edge. [Colour figure can be viewed at wileyonlinelibrary.com]

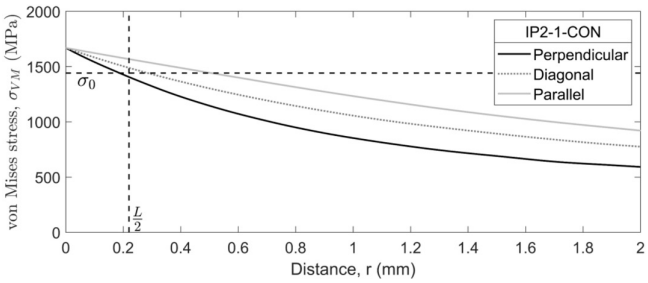

FIGURE 11 | Application of the TCD-PM to the stress–distance curves extracted along different focus path directions for representative CON inner plate.

$$\text{Relative prediction error}\,(\%) = \frac{\sigma_{\text{eff}} - \sigma_0}{\sigma_0} \times 100. \tag{3}$$

A representative example for the CON inner plates' plots (IP2-1-CON) is shown in Figure 11. The results, summarized in Table 4, report the crack path orientation predicted from the failure mode according to BS EN 1993-1-8 (hereafter referred to as EC3-1-8) [32], the experimentally observed crack paths, and the stress–distance results obtained from the perpendicular, diagonal, and parallel focus paths. The values corresponding to the observed crack paths are highlighted in dark gray. Across all CON plates, the extraction path parallel to the loading direction consistently produced the highest effective stress, σ_{eff}. This is largely in agreement with both the EC3-1-8 predictions [32] and the observed crack paths (Table 4).

The overall accuracy of the PM associated with the considered focus paths was assessed in terms of the mean absolute error (MAE), defined as follows:

$$\text{MAE}(\%) = \frac{1}{n}\sum_{i=1}^{n}\left|\text{Relative prediction error}_i\right| \tag{4}$$

where n is the number of estimates. Based on the error index, the perpendicular path provided the highest level of accuracy with a combined MAE across all single- and double-bolt configurations of 8.0%, outperforming the diagonal path with an MAE of 9.1% and the parallel path with an MAE of 12.8%. However, the perpendicular direction showed a slightly higher tendency toward nonconservative predictions, particularly for several double-bolted configuration specimens. It was also evident that selecting the extraction direction to match the observed crack propagation direction did not improve the overall accuracy (combined MAE = 8.7%), relative to using the perpendicular direction.

Regarding the obtained accuracy as a function of the adopted focus path, it is important to note that the TCD generally provides estimates that fall within an error interval of ±20% [18, 21]. Because, apart from a small number of outliers, most results across all directions lie within this ±20% error band (Table 4), this indicates that the differences between the effective stresses associated with the three potential directions fall within the intrinsic accuracy of the TCD. This suggests that the most appropriate way to apply the TCD is to identify the focus path associated with the maximum damage extent, which generally returns a crack propagation direction that is well aligned with the one identified using the EC3-1-8 standard approach [32] (Table 4).

Turning back to the calibration of the TCD, the relatively low MAE suggests that the values of σ_0 and L derived from idealized CON notched specimens are adequate for the CON inner plate connections, despite the greater complexity of the local stress distributions characterizing the tested bolted specimens. That said, coupon tests showed that the material properties differ between manufacturing procedures, and AM-specific process and surface conditions were found to influence crack propagation in WAAM specimens extracted in the diagonal direction [13]. Therefore, the applicability of the adopted σ_0–L pairing to inner plates manufactured by WAAM and SLM deserves to be explored in detail. This will be addressed in the following section.

4.5 | TCD-PM Assessment of WAAM and SLM Inner Plates Using the σ_0–L Pairing Calibrated From CON Notched Specimens

This section examines the accuracy of the PM, calibrated using the σ_0 and L values obtained from the CON notched specimens, in estimating the static strength of bolted joints containing additively manufactured inner plates. This validation exercise is particularly challenging, since the PM was used to postprocess the results from FE models in which the material was modeled as homogeneous and isotropic, that is, without accounting for the manufacturing direction in the stress analysis.

Representative stress–distance plots are shown in Figure 12 for the 2-mm AM plates, including machined WAAM (WAAM-M), machined SLM (SLM-M), and as-built SLM (SLM-AB). Figure 13

TABLE 4 | Accuracy of TCD-PM applied to the CON inner plates (BT: block tearing; EB: edge bearing; NST: net section tension); the dark gray highlighted values indicate the results corresponding to the experimentally observed crack path for each specimen.

	Predicted crack path according to EC3-1-8		Perpendicular path direction		Diagonal path direction		Parallel path direction	
Designation	Failure mode/ crack path	Actual crack path	Effective stress, σ_{eff} (MPa)	Relative prediction error, %	Effective stress, σ_{eff} (MPa)	Relative prediction error, %	Effective stress, σ_{eff} (MPa)	Relative prediction error, %
IP1-1-CON	EB/parallel	Parallel	1769	22.8	1758	22.0	1868	29.6
IP1-2-CON	EB/parallel	Perpendicular	1721	19.4	1682	16.7	1759	22.1
IP1-3-CON	EB/parallel	Parallel	1598	10.9	1571	9.0	1664	15.4
IP1-4-CON	EB/parallel	Parallel	1357	−5.8	1335	−7.3	1420	−1.5
IP1-5-CON	NST/perpendicular	Perpendicular	1373	−4.7	1562	8.1	1642	14.0
IP2-1-CON	BT/perpendicular & parallel	Perpendicular[a]	1406	−2.5	1489	3.3	1568	8.8
IP2-2-CON	BT/perpendicular & parallel	Perpendicular[a]	1376	−4.5	1473	2.2	1567	8.8
IP2-3-CON	EB/parallel	Parallel	1390	−3.5	1408	−2.3	1557	8.0
IP2-4-CON	EB/parallel	Perpendicular[a]	1408	−2.3	1403	−2.7	1482	2.8
IP2-5-CON	EB/parallel	Parallel	1365	5.3	1356	−5.9	1463	1.5
IP2-6-CON	NST/perpendicular	Perpendicular	1514	5.1	1689	17.2	1770	22.9
IP2-7-CON	BT/perpendicular & parallel	Perpendicular[a]	1582	9.8	1628	12.9	1704	18.2

[a]The visible crack initiation/propagation is between the holes.

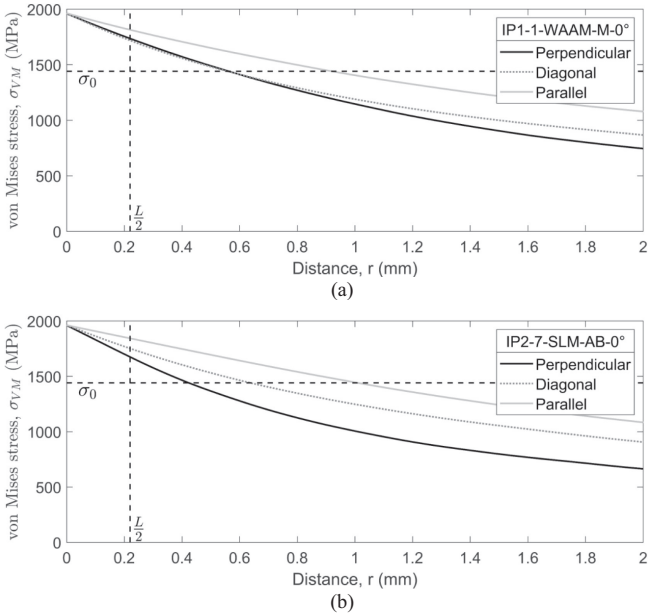

FIGURE 12 | TCD-PM applied to the stress–distance curves extracted along different focus path directions for AM inner plates with a consistent thickness of 2 mm; (a) IP1-1-WAAM-M-0°, representing a single-bolted inner plate, and (b) IP2-7-SLM-M-0°, representing a double-bolted inner plate.

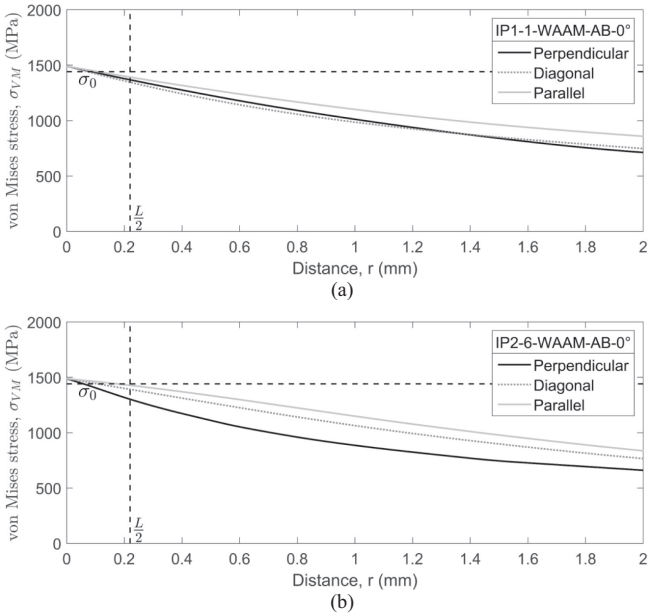

FIGURE 13 | TCD-PM applied to the stress–distance curves extracted along different focus path directions for WAAM-AB inner plates with thicknesses greater than 2 mm; (a) IP1-1-WAAM-AB-0°, representing a single-bolted inner plate, and (b) IP2-7-WAAM-AB-0°, representing a double-bolted inner plate.

presents the corresponding plots for the as-built WAAM (WAAM-AB) plates. The associated TCD prediction results are summarized in Table 5 for the 2-mm AM plates and in Table 6 for the WAAM-AB plates.

In terms of predictive performance for the 2-mm AM plates, the diagonal direction produced the lowest error, with an MAE of 11.7%, closely followed by the perpendicular direction with an MAE of 11.8%, whereas the parallel direction showed a higher error, with an MAE of 15.7%. Consistent with the CON assessment, the perpendicular direction exhibited the strongest tendency toward nonconservative predictions. In addition, selecting the extraction direction to follow the observed crack path slightly lowered the overall accuracy, giving an MAE of 12.9%. Furthermore, it was evident that a small number of prediction errors across all paths fall outside the ± 20% interval, with the outliers predominantly positive, indicating conservative predictions. Compared with the CON plates, the 2-mm AM results show a modest increase in error. However, the level of accuracy remains comparable, indicating that the CON calibrated TCD-PM provides an acceptable prediction for AM inner plates of matched thickness.

In contrast, the WAAM-AB plates with thicknesses exceeding 2 mm showed a reduction in accuracy. The MAE exceeded the 20% threshold for both the perpendicular and diagonal extraction paths, reaching 21.9% and 20.8%, respectively. Although the parallel path showed a slightly lower MAE of 18.4%, all predictions remained nonconservative. A further increase in error was observed for the double-bolt configurations, with MAE rising from 18.6%, 17.5%, and 14.6% for IP1 to 24.9%, 23.8%, and 21.9% for IP2 in the perpendicular, diagonal, and parallel paths, respectively, confirming an evident effect of joint configuration in the as-built plates. When the extraction path corresponding to the experimentally observed crack path was considered, the resulting MAE was approximately 21.1%.

Overall, the accuracy in estimating the static strength of bolted joints containing AM plates was found to decrease. This reduction can be attributed to two main factors: first, AM metals exhibit mechanical properties and microstructural/mesostructural morphologies that differ from those of their conventionally manufactured counterparts, leading to different values of the TCD material constants; second, the FE models did not explicitly account for the microstructural/mesostructural variations associated with the AM process. This is particularly evident for the WAAM-AB plates, where the as-built surface condition induces local geometric irregularities that, together with the anisotropic material response arising from the AM micro/meso-structural morphology, may influence the local process zone ahead of the crack initiation region. These features are not explicitly represented in the simplified linear elastic FE models, which treat the material as homogeneous and isotropic and idealize the local geometry around the bolt hole. Therefore, the remaining nonconservatism should not be interpreted as a thickness effect alone, but rather as a consequence of the WAAM-AB morphology and its associated anisotropic material behavior not being fully captured by the adopted FE/TCD framework. Nevertheless, despite these complexities and modeling limitations, the accuracy obtained using TCD parameters calibrated from conventionally manufactured material remains remarkable, with prediction errors still close to the typical ±20% range commonly observed when the TCD is applied to a variety of structural integrity problems [18, 21].

TABLE 5 | Accuracy of TCD-PM applied to the AM inner plates with a consistent thickness of 2 mm (BT: block tearing; EB: edge bearing; NST: net section tension); the dark gray highlighted values indicate the results corresponding to the experimentally observed crack path for each specimen.

Designation	Predicted crack path according to EC3-1-8 Failure mode/ crack path	Actual crack path	Perpendicular path direction Effective stress, σ_{eff} (MPa)	Perpendicular path direction Relative prediction error, %	Diagonal path direction Effective stress, σ_{eff} (MPa)	Diagonal path direction Relative prediction error, %	Parallel path direction Effective stress, σ_{eff} (MPa)	Parallel path direction Relative prediction error, %
IP1-1-WAAM-M-0°	EB/parallel	Parallel	1737	20.6	1718	19.2	1816	26.1
IP1-1-WAAM-M-45°	EB/parallel	Diagonal	1807	25.4	1786	23.9	1890	31.2
IP1-1-WAAM-M-60°	EB/parallel	Diagonal	1744	21.1	1725	19.7	1825	26.6
IP1-1-WAAM-M-90°	EB/parallel	Parallel	1691	17.4	1673	16.1	1767	22.6
IP1-2-WAAM-M-0°	EB/parallel	Parallel	1614	12.0	1579	9.6	1649	14.5
IP1-2-WAAM-M-45°	EB/parallel	Diagonal	1803	25.2	1763	22.4	1843	27.9
IP1-2-WAAM-M-60°	EB/parallel	Diagonal	1724	19.6	1686	17.0	1762	22.3
IP1-2-WAAM-M-90°	EB/parallel	Parallel	1558	8.1	1525	5.8	1591	10.4
IP1-3-WAAM-M-0°	EB/parallel	Parallel	1532	6.3	1506	4.5	1593	10.5
IP1-4-WAAM-M-0°	EB/parallel	Parallel	1346	−6.6	1325	−8.1	1406	−2.4
IP1-1-SLM-M-0°	EB/parallel	Parallel	1744	21.1	1725	19.7	1825	26.6
IP1-1-SLM-AB-0°	EB/parallel	Parallel	1763	22.4	1743	21.0	1844	28.0
IP1-2-SLM-AB-0°	EB/parallel	Parallel	1743	20.9	1705	18.3	1781	23.6
IP1-2-SLM-AB-45°	EB/parallel	Parallel	1788	24.1	1750	21.5	1827	26.8
IP1-2-SLM-AB-90°	EB/parallel	Parallel	1676	16.3	1640	13.8	1712	18.8
IP1-5-SLM-AB-0°	NST/perpendicular	Perpendicular	1331	−7.7	1510	4.8	1591	10.4
IP1-5-SLM-AB-45°	NST/perpendicular	Perpendicular	1272	−11.7	1444	0.2	1519	5.4
IP1-5-SLM-AB-90°	NST/perpendicular	Perpendicular	1224	−15.0	1390	−3.6	1462	1.5
IP2-1-WAAM-M-0°	BT/perpendicular & parallel	Perpendicular[a]	1333	−7.5	1370	−4.9	1437	−0.3
IP2-1-WAAM-M-45°	BT/perpendicular & parallel	Diagonal	1495	3.7	1516	5.2	1623	12.7

(Continues)

TABLE 5 | (Continued)

Designation	Predicted crack path according to EC3-1-8 Failure mode/ crack path	Actual crack path	Perpendicular path direction Effective stress, σ_{eff} (MPa)	Perpendicular path direction Relative prediction error, %	Diagonal path direction Effective stress, σ_{eff} (MPa)	Diagonal path direction Relative prediction error, %	Parallel path direction Effective stress, σ_{eff} (MPa)	Parallel path direction Relative prediction error, %
IP2-1-WAAM-M-60°	BT/perpendicular & parallel	Diagonal[a]	1356	−5.9	1395	−3.2	1464	1.6
IP2-1-WAAM-M-90°	BT/perpendicular & parallel	Perpendicular[a]	1287	−10.7	1323	−8.2	1386	−3.8
IP2-2-WAAM-M-0°	BT/perpendicular & parallel	Parallel	1511	4.8	1509	4.7	1613	12.0
IP2-3-WAAM-M-0°	BT/perpendicular & parallel	Parallel	1452	0.7	1452	0.7	1572	9.1
IP2-3-WAAM-M-45°	EB + BT/ perpendicular & parallel	Diagonal	1483	2.9	1483	2.9	1610	11.7
IP2-3-WAAM-M-60°	BT/perpendicular & parallel	Diagonal	1419	−1.5	1419	−1.5	1538	6.7
IP2-3-WAAM-M-90°	BT/perpendicular & parallel	Parallel	1324	−8.1	1324	−8.1	1430	−0.7
IP2-4-WAAM-M-0°	BT/perpendicular & parallel	Parallel	1411	−2.1	1409	−2.2	1529	6.1
IP2-5-WAAM-M-0°	EB/parallel	Parallel	1309	−9.2	1277	−11.4	1328	−7.8
IP2-7-WAAM-M-0°	BT/perpendicular & parallel	Perpendicular[a]	1575	9.3	1643	14.0	1731	20.2
IP2-7-SLM-M-0°	BT/perpendicular & parallel	Perpendicular[a]	1588	10.2	1656	14.9	1747	21.2
IP2-6-SLM-AB-0°	NST/perpendicular	Perpendicular	1537	6.6	1707	18.4	1787	24.0
IP2-6-SLM-AB-45°	NST/perpendicular	Perpendicular	1563	8.4	1734	20.4	1814	25.9
IP2-6-SLM-AB-90°	NST/perpendicular	Perpendicular	1514	5.0	1680	16.6	1757	21.9
IP2-7-SLM-AB-0°	BT/perpendicular & parallel	Perpendicular[a]	1678	16.5	1750	21.5	1845	28.1

[a]The visible crack initiation/propagation is between the holes.

TABLE 6 | Accuracy of TCD-PM applied to the AM inner plates with thicknesses greater than 2 mm (BT: block tearing; EB: edge bearing; NST: net section tension); the dark gray highlighted values indicate the results corresponding to the experimentally observed crack path for each specimen.

Designation	Predicted crack path according to EC3-1-8 Failure mode/ crack path	Actual crack path	Perpendicular path direction		Diagonal path direction		Parallel path direction	
			Effective stress, σ_{eff} (MPa)	Relative prediction error, %	Effective stress, σ_{eff} (MPa)	Relative prediction error, %	Effective stress, σ_{eff} (MPa)	Relative prediction error, %
IP1-1-WAAM-AB-0°	EB/parallel	Parallel	1368	−5.1	1345	−6.6	1393	−3.3
IP1-2-WAAM-AB-0°	EB/parallel	Parallel	1299	−9.8	1275	−11.5	1322	−8.3
IP1-2-WAAM-AB-45°	EB/parallel	Diagonal	1354	−6.0	1327	−7.9	1377	−4.4
IP1-2-WAAM-AB-60°	EB/parallel	Diagonal	1255	−12.9	1232	−14.5	1279	−11.2
IP1-2-WAAM-AB-90°	EB/parallel	Parallel	1386	−3.8	1362	−5.5	1411	−2.1
IP1-3-WAAM-AB-0°	EB/parallel	Parallel	1183	−17.9	1157	−19.7	1204	−16.5
IP1-4-WAAM-AB-0°	EB/parallel	Parallel	1011	−29.8	997	−30.8	1039	−27.9
IP1-5-WAAM-AB-0°	NST/perpendicular	Perpendicular	1035	−28.2	1122	−22.1	1159	−19.6
IP1-5-WAAM-AB-45°	NST/perpendicular	Perpendicular	1055	−26.8	1144	−20.6	1178	−18.3
IP1-5-WAAM-AB-60°	NST/perpendicular	Perpendicular	920	−36.1	996	−30.9	1028	−28.7
IP1-5-WAAM-AB-90°	NST/perpendicular	Perpendicular	1033	−28.3	1121	−22.2	1155	−19.8
IP2-2-WAAM-AB-0°	BT/perpendicular & parallel	Perpendicular[a]	1045	−27.5	1045	−27.5	1072	−25.6
IP2-3-WAAM-AB-0°	BT/perpendicular & parallel	Parallel	951	−34.0	926	−35.7	943	−34.6
IP2-3-WAAM-AB-45°	BT/perpendicular & parallel	Diagonal	994	−31.0	965	−33.0	984	−31.7
IP2-3-WAAM-AB-60°	BT/perpendicular & parallel	Diagonal	957	−33.6	929	−35.5	949	−34.2
IP2-3-WAAM-AB-90°	BT/perpendicular & parallel	Parallel	881	−38.8	856	−40.6	873	−39.4
IP2-4-WAAM-AB-0°	BT/perpendicular & parallel	Parallel	1040	−27.9	1010	−29.9	1032	−28.4

(Continues)

TABLE 6 | (Continued)

Designation	Predicted crack path according to EC3-1-8		Perpendicular path direction		Diagonal path direction		Parallel path direction	
	Failure mode/ crack path	Actual crack path	Effective stress, σ_{eff} (MPa)	Relative prediction error, %	Effective stress, σ_{eff} (MPa)	Relative prediction error, %	Effective stress, σ_{eff} (MPa)	Relative prediction error, %
IP2-5-WAAM-AB-0°	BT/perpendicular & parallel	Parallel	973	−32.5	952	−33.9	972	−32.5
IP2-6-WAAM-AB-0°	NST/perpendicular	Perpendicular	1301	−9.7	1392	−3.4	1427	−1.0
IP2-6-WAAM-AB-45°	NST/perpendicular	Perpendicular	1251	−13.2	1336	−7.3	1373	−4.7
IP2-6-WAAM-AB-60°	NST/perpendicular	Perpendicular	1156	−19.8	1241	−13.9	1274	−11.6
IP2-6-WAAM-AB-90°	NST/perpendicular	Perpendicular	1227	−14.8	1308	−9.2	1342	−6.8
IP2-7-WAAM-AB-0°	BT/perpendicular & parallel	Perpendicular	1215	−15.7	1222	−15.2	1265	−12.2

[a]The visible crack initiation/propagation is between the holes.

4.6 | TCD-PM Assessment of WAAM-AB Inner Plates Using σ_0-L Under the Same AM Conditions

With the decrease in the PM prediction accuracy observed for the combined results of both single- and double-bolt configurations of the WAAM-AB plates, a further investigation was carried out by exploring an alternative calibration strategy. As shown in Table 7, calibrating the σ_0-L pairing from the WAAM-AB notched specimens slightly improved the PM accuracy. The MAE decreased to 19.7%, 18.1%, and 15.3% for the perpendicular, diagonal, and parallel extraction paths, respectively, meaning that the majority of the results from all three directions fall within the ±20% interval. However, the double-bolt configurations generally showed larger errors than the single-bolt plates, indicating that the joint configuration in WAAM-AB specimens still affects the prediction accuracy even after calibration based on matching mean thickness. Moreover, the predictions remained predominantly nonconservative, with negative accuracy values governing the results, although a few cases became slightly conservative, reaching up to 4.1%. Despite these complexities, the results discussed in this section indicate that using a σ_0–L pairing calibrated from notched WAAM-AB specimens yields a modest improvement in prediction accuracy.

To account for the limited number of WAAM-AB notched specimens used for calibration, a sensitivity check was also performed by varying σ_0 by ±5% while keeping L unchanged. This analysis showed a noticeable shift in the prediction errors, confirming that the recalibrated predictions are sensitive to the selected value of σ_0. However, the predictions remained predominantly nonconservative, and the overall trend was not removed. Therefore, the recalibrated assessment should be interpreted as an indicative evaluation of the benefit of using WAAM-AB specific calibration parameters, rather than as a statistically robust calibration.

4.7 | Comparison Between TCD-PM and EC3-1-8 Resistance Predictions

A detailed assessment of resistance predictions according to EC3-1-8 [32] for the tested hybrid bolted joints was reported in a separate study [33], where the relevant resistance equations, failure estimations, and comparisons with other design provisions were discussed. Therefore, the present section compares the EC3-1-8 [32] resistance predictions with the TCD-PM predictions in terms of failure load. The comparison is based on the experimental-to-predicted failure load ratio, where values greater than unity indicate conservative predictions and values lower than unity indicate nonconservative predictions.

As seen in Figure 14a,b, the TCD-PM predictions, in terms of mean load ratios, were close to unity for the CON plates. However, except for the perpendicular path in the double-bolt configuration, all paths showed nonconservative predictions compared with EC3-1-8 [32]. Moreover, the TCD-PM predictions had a slightly higher coefficient of variation (COV) for the single-bolt configuration but an evidently lower COV for the double-bolt configuration.

In contrast, the TCD-PM predictions for the AM plates, shown in Figure 14c,d, were generally slightly conservative,

TABLE 7 | Accuracy of TCD-PM applied to the AM inner plates with thicknesses greater than 2 mm using the WAAM-AB calibrated σ_0–L pairing (BT: block tearing; EB: edge bearing; NST: net section tension); the dark gray highlighted values indicate the results corresponding to the experimentally observed crack path for each specimen.

Designation	Predicted crack path according to EC3-1-8 Failure mode/ crack path	Actual crack path	Perpendicular path direction		Diagonal path direction		Parallel path direction	
			Effective stress, σ_{eff} (MPa)	Relative prediction error, %	Effective stress, σ_{eff} (MPa)	Relative prediction error, %	Effective stress, σ_{eff} (MPa)	Relative prediction error, %
IP1-1-WAAM-AB-0°	EB/parallel	Parallel	1321	−1.8	1292	−3.9	1354	0.7
IP1-2-WAAM-AB-0°	EB/parallel	Parallel	1255	−6.7	1225	−9.0	1285	−4.5
IP1-2-WAAM-AB-45°	EB/parallel	Diagonal	1307	−2.8	1275	−5.2	1339	−0.5
IP1-2-WAAM-AB-60°	EB/parallel	Diagonal	1212	−9.9	1183	−12.1	1243	−7.6
IP1-2-WAAM-AB-90°	EB/parallel	Parallel	1341	−0.3	1310	−2.6	1374	2.1
IP1-3-WAAM-AB-0°	EB/parallel	Parallel	1142	−15.1	1113	−17.2	1170	−13.0
IP1-4-WAAM-AB-0°	EB/parallel	Parallel	974	−27.6	956	−28.9	1012	−24.8
IP1-5-WAAM-AB-0°	NST/perpendicular	Perpendicular	976	−27.4	1088	−19.1	1135	−15.6
IP1-5-WAAM-AB-45°	NST/perpendicular	Perpendicular	993	−26.2	1111	−17.4	1157	−13.9
IP1-5-WAAM-AB-60°	NST/perpendicular	Perpendicular	867	−35.5	970	−27.9	1010	−24.9
IP1-5-WAAM-AB-90°	NST/perpendicular	Perpendicular	973	−27.7	1091	−18.9	1136	−15.6
IP2-2-WAAM-AB-0°	BT/perpendicular & parallel	Perpendicular[a]	1005	−25.3	1007	−25.2	1043	−22.5
IP2-3-WAAM-AB-0°	BT/perpendicular & parallel	Parallel	925	−31.2	892	−33.7	914	−32.0
IP2-3-WAAM-AB-45°	BT/perpendicular & parallel	Diagonal	965	−28.2	930	−30.9	955	−29.0
IP2-3-WAAM-AB-60°	BT/perpendicular & parallel	Diagonal	930	−30.8	895	−33.5	918	−31.7

(Continues)

TABLE 7 | (Continued)

Designation	Predicted crack path according to EC3-1-8 Failure mode/ crack path	Actual crack path	Perpendicular path direction Effective stress, σ_{eff} (MPa)	Perpendicular path direction Relative prediction error, %	Diagonal path direction Effective stress, σ_{eff} (MPa)	Diagonal path direction Relative prediction error, %	Parallel path direction Effective stress, σ_{eff} (MPa)	Parallel path direction Relative prediction error, %
IP2-3-WAAM-AB-90°	BT/perpendicular & parallel	Parallel	858	−36.2	826	−38.6	846	−37.1
IP2-4-WAAM-AB-0°	BT/perpendicular & parallel	Parallel	1009	−25.0	973	−27.7	1000	−25.7
IP2-5-WAAM-AB-0°	BT/perpendicular & parallel	Parallel	944	−29.8	916	−31.9	943	−29.9
IP2-6-WAAM-AB-0°	NST/perpendicular	Perpendicular	1234	−8.3	1352	0.5	1400	4.1
IP2-6-WAAM-AB-45°	NST/perpendicular	Perpendicular	1185	−11.9	1298	−3.5	1345	0
IP2-6-WAAM-AB-60°	NST/perpendicular	Perpendicular	1095	−18.6	1203	−10.6	1247	−7.3
IP2-6-WAAM-AB-90°	NST/perpendicular	Perpendicular	1164	−13.5	1271	−5.5	1316	−2.2
IP2-7-WAAM-AB-0°	BT/perpendicular & parallel	Perpendicular	1164	−13.5	1177	−12.5	1236	−8.1

[a]The visible crack initiation/propagation is between the holes.

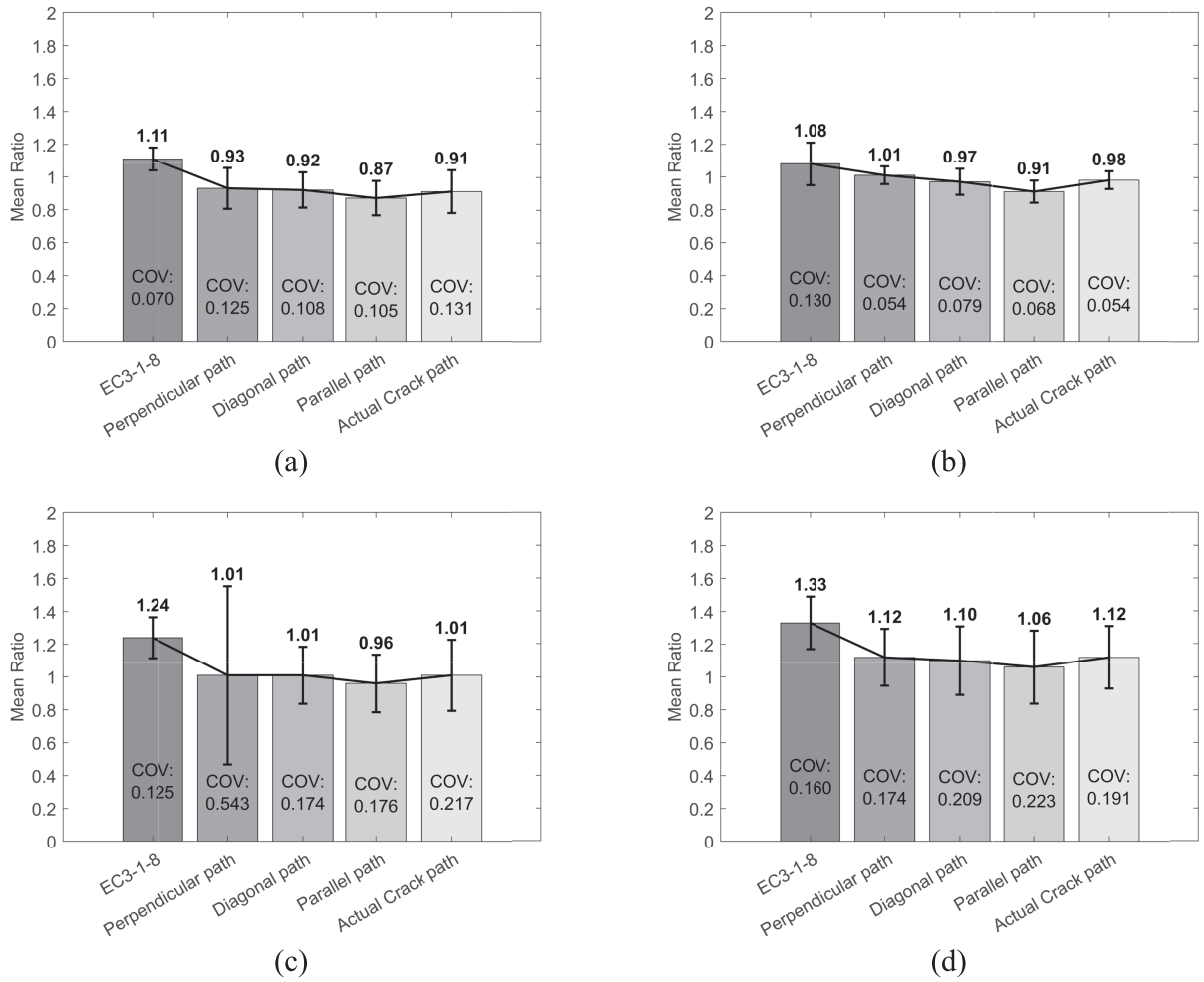

FIGURE 14 | Comparison between EC3-1-8 [32] and TCD-PM failure load predictions using different stress extraction paths against experimental failure loads: mean experimental-to-predicted load ratios and COV of CON plates in (a) single- and (b) double-bolt configurations and AM plates in (c) single- and (d) double-bolt configurations.

with mean ratios mostly higher than unity for the single-bolt AM plates and between 1.06 and 1.12 for the double-bolt AM plates. However, the TCD-PM results showed greater scatter, especially for the perpendicular path in the single-bolt configuration, reflecting the sensitivity of the method to the selected extraction path and to local material and geometrical variability. Overall, EC3-1-8 [32] provides a conservative design baseline, whereas TCD-PM gives closer mean failure load predictions.

5 | Concluding Remarks

Based on the static tests, linear elastic FE models, and the PM analysis, it can be concluded that

1. Linear elastic FE models of the conventional and additively manufactured notched specimens and bolted joints captured the stress fields required for the TCD assessments. The predictions were also insensitive to reasonable variations in mesh density and friction.
2. Applying the PM, when calibrated using the conventional notched plates, provided broadly acceptable predictions for additively manufactured inner plates of matched thickness.
3. For the as-built WAAM inner plates with mean thicknesses greater than 2 mm, using the calibration obtained from the conventional notched plates led to a clear reduction in accuracy and nonconservative predictions for all specimens. This confirms that the PM formulation is sensitive to the values of the calibration material properties being used.
4. Recalibrating the material parameters using as-built WAAM notched specimens improved the predictions for the as-built WAAM inner plates and moved the overall MAE across all stress–distance paths back within an acceptable error range, although a nonconservative tendency remained.
5. Double-bolt configuration as-built WAAM inner plates showed larger errors than the single-bolt specimens even after the recalibration process, indicating that joint configuration influences prediction accuracy.

6. The most accurate stress extraction path varied between specimen groups, with no single path giving both the lowest error and consistently conservative predictions. Therefore, when the actual cracking behavior is not known, the path providing the most conservative results should be adopted.
7. Compared with EC3-1-8 [32], the PM gave mean ratios closer to unity but was generally less conservative and sensitive to the selected extraction path.

Author Contributions

Hasan Almuhanna: writing – original draft, investigation, methodology, formal analysis. **Giacomo Torelli:** writing – review and editing, supervision. **Luca Susmel:** writing – original draft, writing – review and editing, supervision, methodology, conceptualization.

Acknowledgments

This work was supported by the Henry Royce Institute for Advanced Materials, funded through Engineering and Physical Sciences Research Council grants EP/R00661X/1, EP/P025021/1, and EP/S019367/1. The authors would also like to acknowledge the Kuwait Institute for Scientific Research (KISR) for funding the tuition fees of the lead author's PhD program.

Funding

This work was supported by the Henry Royce Institute for Advanced Materials, funded through Engineering and Physical Sciences Research Council grants EP/R00661X/1, EP/P025021/1, and EP/S019367/1. The authors would also like to acknowledge the Kuwait Institute for Scientific Research (KISR) for funding the tuition fees of the lead author's PhD program.

Data Availability Statement

Data will be made available on request.

References

1. Y. Liu, J. Ye, Y. Yang, et al., "Experimental Study on Wire and Arc Additively Manufactured Steel Double-Shear Bolted Connections," *Journal of Building Engineering* 76 (2023): 107330, https://doi.org/10.1016/j.jobe.2023.107330.

2. X. Guo, P. Kyvelou, J. Ye, L. H. Teh, and L. Gardner, "Experimental Study of DED-Arc Additively Manufactured Steel Double-Lap Shear Bolted Connections," *Engineering Structures* 281 (2023): 115736, https://doi.org/10.1016/j.engstruct.2023.115736.

3. Z. Kong, R. Li, X. Wang, et al., "Shear Capacity of Additively Manufactured Stainless Steel Bolted Connections After Fire," *Engineering Structures* 322 (2025): 119102, https://doi.org/10.1016/j.engstruct.2024.119102.

4. W. Zuo, M. T. Chen, O. Zhao, et al., "Structural Performance of Wire Arc Additively Manufactured Duplex Stainless Steel Single-Lap Shear Bolted Connections," *Engineering Structures* 319 (2024): 118706, https://doi.org/10.1016/j.engstruct.2024.118706.

5. Y. Liu, J. Ye, J. He, et al., "Testing and Design of Wire and Arc Additively Manufactured Steel Double-Shear Bolted Connections With Thick Plates," *Journal of Constructional Steel Research* 224 (2025): 109069, https://doi.org/10.1016/j.jcsr.2024.109069.

6. W. Zuo, M. T. Chen, O. Zhao, et al., "Behavior of Wire Arc Additively Manufactured 316L Austenitic Stainless Steel Single Shear Bolted Connections," *Thin-Walled Structures* 202 (2024): 112075, https://doi.org/10.1016/j.tws.2024.112075.

7. X. Guo, P. Kyvelou, J. Ye, L. H. Teh, and L. Gardner, "Experimental Investigation of Wire Arc Additively Manufactured Steel Single-Lap Shear Bolted Connections," *Thin-Walled Structures* 181 (2022): 110029, https://doi.org/10.1016/j.tws.2022.110029.

8. W. Zuo, M. T. Chen, S. W. Liu, et al., "Experimental Investigation on Double-Lap Shear Behavior of 3D Printed Austenitic Stainless Steel Bolted Connections," *Engineering Structures* 317 (2024): 118501, https://doi.org/10.1016/j.engstruct.2024.118501.

9. B. Gil, R. Goñi, M. Fábregas, and E. Bayo, "Design and Testing of Steel Additive-Manufactured Moment-Resistant Beam-To-Column Connection," *Journal of Constructional Steel Research* 219 (2024): 108747, https://doi.org/10.1016/j.jcsr.2024.108747.

10. M. Erven, J. Lange, and T. Feucht, "3D-Printing With Steel of a Bolted Connection," *Ce/papers* 4 (2021): 825–832, https://doi.org/10.1002/cepa.

11. C. Xie, A. Bagheri Sabbagh, E. Bakhshivand, and O. Iuorio, "Shape Optimisation of Metal Additive Manufacturing Connections in Lightweight Steel Structures," *Journal of Constructional Steel Research* 241 (2026): 110290, https://doi.org/10.1016/j.jcsr.2026.110290.

12. Z. Zhang, F. He, Z. Chen, et al., "Comprehensive Review of Robotic Wire Arc Additive Manufacturing for Steel Structures: Process, Material Behaviour, Structural Applications and Pathways to Automated Construction," *Automation in Construction* 182 (2026): 106758, https://doi.org/10.1016/j.autcon.2025.106758.

13. H. Almuhanna, G. Torelli, R. Kindermann, and L. Susmel, "Failure Investigation of Hybrid Double-Lap Shear Bolted Connections With Additively Manufactured 316L Stainless Steel Inner Plates," *Engineering Failure Analysis* 179 (2025): 109756, https://doi.org/10.1016/J.ENGFAILANAL.2025.109756.

14. K. Jiang and O. Zhao, "Ferritic Stainless Steel Thin Sheet Bolted Connections Failing by Bearing–Curling Interaction: Testing, Modelling and Design," *Engineering Structures* 283 (2023): 115919, https://doi.org/10.1016/j.engstruct.2023.115919.

15. H. Wen and H. Mahmoud, "Strength Determination and Fracture Characteristics of Bolted Connections," *Journal of Structural Engineering* 147 (2021): 04021132, https://doi.org/10.1061/(asce)st.1943-541x.0003076.

16. D. Taylor, *The Theory of Critical Distances: A New Perspective in Fracture Mechanics* (Elsevier Science, 2007).

17. T. Alena, A. Kostina, P. Oleg, and S. Luca, "Elasto-Plastic TCD as a Method of Failure Prediction," in *Procedia Structural Integrity*, 5 (Elsevier B.V, 2017), 569–576, https://doi.org/10.1016/j.prostr.2017.07.174.

18. L. Susmel and D. Taylor, "On the Use of the Theory of Critical Distances to Predict Static Failures in Ductile Metallic Materials Containing Different Geometrical Features," *Engineering Fracture Mechanics* 75 (2008): 4410–4421, https://doi.org/10.1016/j.engfracmech.2008.04.018.

19. L. Susmel and D. Taylor, "The Theory of Critical Distances to Estimate the Static Strength of Notched Samples of Al6082 Loaded in Combined Tension and Torsion. Part I: Material Cracking Behaviour," *Engineering Fracture Mechanics* 77 (2010): 452–469, https://doi.org/10.1016/j.engfracmech.2009.11.015.

20. L. Susmel and D. Taylor, "The Theory of Critical Distances to Estimate the Static Strength of Notched Samples of Al6082 Loaded in Combined Tension and Torsion. Part II: Multiaxial Static Assessment," *Engineering Fracture Mechanics* 77 (2010): 470–478, https://doi.org/10.1016/j.engfracmech.2009.10.004.

21. A. A. H. Ameri, J. B. Davison, and L. Susmel, "On the Use of Linear-Elastic Local Stresses to Design Load-Carrying Fillet-Welded Steel Joints Against Static Loading," *Engineering Fracture Mechanics* 136 (2015): 38–57, https://doi.org/10.1016/j.engfracmech.2015.02.004.

22. A. A. Ahmed and L. Susmel, "Static Assessment of Plain/Notched Polylactide (PLA) 3D-Printed With Different Infill Levels: Equivalent

Homogenised Material Concept and Theory of Critical Distances," *Fatigue and Fracture of Engineering Materials and Structures* 42 (2019): 883–904, https://doi.org/10.1111/ffe.12958.

23. L. Susmel and D. Taylor, "The Theory of Critical Distances to Predict Static Strength of Notched Brittle Components Subjected to Mixed-Mode Loading," *Engineering Fracture Mechanics* 75 (2008): 534–550, https://doi.org/10.1016/j.engfracmech.2007.03.035.

24. D. Lobanov, A. Yankin, M. Mullahmetov, E. Chebotareva, and V. Melnikova, "The Analysis of Stress Raisers Affecting the GFRP Strength at Quasi-Static and Cyclic Loads by the Theory of Critical Distances, Digital Image Correlation, and Acoustic Emission," *Polymers (Basel)* 15 (2023): 2087, https://doi.org/10.3390/polym15092087.

25. ASTM E8/E8M, *Standard Test Methods for Tension Testing of Metallic Materials* (International and American Society for Testing Materials, 2024).

26. D. Taylor, "Predicting the Fracture Strength of Ceramic Materials Using the Theory of Critical Distances," *Engineering Fracture Mechanics* 71 (2004): 2407–2416, https://doi.org/10.1016/j.engfracmech.2004.01.002.

27. L. Marsavina, A. Sapora, L. Susmel, and D. Taylor, "The Application of the Theory of Critical Distances to Nonhomogeneous Materials," *Fatigue and Fracture of Engineering Materials and Structures* 46 (2023): 1314–1329, https://doi.org/10.1111/ffe.13922.

28. ASTM, *E399, Standard Test Method for Linear-Elastic Plane-Strain Fracture Toughness of Metallic Materials* (ASTM, 2023).

29. ANSYS Inc, *ANSYS® Academic Research Mechanical (n.d.)* (ANSYS Inc, 2023), https://www.ansys.com/products/academic.

30. K. F. Chung and K. H. Ip, "Finite Element Modeling of Bolted Connections Between Cold-Formed Steel Strips and Hot Rolled Steel Plates Under Static Shear Loading," *Engineering Structures* 22, no. 10 (2000): 1271–1284, www.elsevier.com/locate/engstruct.

31. S. H. Ju, C. Y. Fan, and G. H. Wu, "Three-Dimensional Finite Elements of Steel Bolted Connections," *Engineering Structures* 26 (2004): 403–413, https://doi.org/10.1016/j.engstruct.2003.11.001.

32. British Standards Institution, *BS EN 1993-1-8, Eurocode 3. Design of Steel Structures. Part 1–8: Joints* (BSI, 2024).

33. H. Almuhanna, G. Torelli, and L. Susmel, "Static Assessment of Hybrid Double-Lap Bolted Joints With Additively Manufactured 316L Plates," *Fatigue and Fracture of Engineering Materials and Structures* 49 (2026): 1721–1741, https://doi.org/10.1111/ffe.70218.